DOI: 10.1002/chem.200800106

Uniform Metal (Hydr)Oxide Particles from Water/Ionic Liquid Precursor (ILP) Mixtures

Zhonghao Li,[a, e] Pierre Rabu,[b] Peter Strauch,[a] Alexandre Mantion,[c, f] and Andreas Taubert*[a, d]

Abstract: We have recently shown that the hydrated ionic liquid tetrabutylammonium hydroxide (TBAH) is an efficient ionic liquid precursor (ILP) for the fabrication of ZnO/carbohydrate materials (D. Mumalo-Djokic, W. B. Stern, A. Taubert, *Cryst. Growth Des.* **2008**, *8*, 330). The current paper shows that ZnO is just one example out of the large group of technologically important metal (hydr)oxides that can be made using TBAH. Simply by using different metal acetates as precursors in TBAH, it is possible to make a wide variety of metal (hydr)oxides with well-defined size, morphology, and chemical composition. It is also possible to dope metal oxide particles or to synthesize mixed metal oxide particles, and therefore to control properties like magnetism.

Keywords: ionic liquids · magnetic properties · nanostructures · oxides · synthesis design

Introduction

Metal (hydr)oxide particles, especially transition metal and doped metal (hydr)oxides with sizes in the low micrometer to nanometer range, are important materials for many applications. Catalysis, magnetic storage, labels and contrast agents for biomedicine, and battery technology are but a few examples of nanoscale metal (hydr)oxide applications.[1] Some compounds like (doped) ZnO have been made successfully and with controllable properties using conventional wet-chemistry or gas-phase approaches.[2–5] Other metal (hydr)oxides have been less straightforward to fabricate and tune with respect to a certain property.

We have earlier demonstrated that CaF_2 tubes,[6] CuCl platelets,[7–9] and Au platelets[10] can be fabricated in a controlled fashion from ionic liquids (ILs) and ionic liquid crystals (ILCs) if the IL or ILC acts as an "all-in-one" solvent–reactant–template for the final product. Unlike regular ILs or ILCs, these special compounds act as the precursor for the inorganic material, the solvent for the reaction, and the template for the final inorganic particle morphology at the same time.[11,12] As a result, such systems have been called ionic liquid precursors (ILPs) or ionic liquid crystal precursors (ILCPs) and the concept has been carried further by several research groups.[13–15] Recently, Zhu et al.[16] and our laboratory[17,18] have shown that the ILP and ILCP concepts are also applicable to the synthesis of technologically important compounds like ZnO.

Furthermore, there have been a few reports showing that inorganic synthesis in ILs occasionally leads to materials that are difficult or impossible to obtain by using other synthesis protocols. For example, Nakashima and Kimizuka have shown that ILs provide easy access to hollow TiO_2 microspheres.[19] Morris and co-workers have demonstrated

[a] Dr. Z. Li, Prof. P. Strauch, Prof. A. Taubert
Institute of Chemistry
University of Potsdam
14476 Golm (Germany)
Fax: (+49) 331-977-5773
E-mail: ataubert@uni-potsdam.de

[b] Dr. P. Rabu
Institut de Physique et Chimie des Matériaux
UMR7504 CNRS-Université Louis Pasteur
67034 Strasbourg (France)

[c] Dr. A. Mantion
Department of Chemistry
University of Basel
4056 Basel (Switzerland)

[d] Prof. A. Taubert
Max-Planck-Institute of Colloids and Interfaces
14476 Golm (Germany)

[e] Dr. Z. Li
Current address: School of Materials Science and Engineering
Shandong University, Jinan
250061 (China)

[f] Dr. A. Mantion
Current address: Department of Chemistry, Humboldt University
Brook-Taylor-Str. 2
12489 Berlin (Germany)

Supporting information for this article is available on the WWW under http://dx.doi.org/10.1002/chem.200800106.

that ionothermal synthesis leads to interesting metal phosphates.[20–25] Smarsly and colleagues have shown that ILs also allow for the low-temperature synthesis of both anatase and rutile by appropriately choosing the reaction conditions.[26] The same authors have also shown that ceria with bimodal pore size distributions and silica with well-defined pores can be grown from ILs.[27–29] Finally, Farag and Endres have shown that ILs also enable the synthesis of different phases of alumina by IL variation.[30]

The current paper shows that ZnO is just one example out of the large group of metal (hydr)oxides that can be made using the ILP or ILCP route. Here we demonstrate that simply by replacing the zinc acetate precursor used in our previous work[17,18] with other metal acetates, it is possible to synthesize a wide variety of metal (hydr)oxides with uniform size, morphology, and chemical composition. It is also possible to dope metal oxides or to produce mixed metal oxide particles. The approach presented here is complementary to an approach reported by Polarz and co-workers, who described the synthesis of well-defined $ZnMnO_3$ and $ZnMn_2O_4$ nanoparticles from a single-source molecular precursor.[31] The advantage of our approach, however, is that there is no need for the synthesis of complex metal organic precursors prior to the metal (hydr)oxides synthesis. Rather, simple salts like metal acetates can be used as precursors for well-defined materials like cobalt ferrite nanoparticles with uniform diameters of a few nanometers.

Results and Discussion

In a typical synthesis, 10 g of tetrabutylammonium hydroxide (TBAH) were heated to 100 °C. Subsequently, 2 mL of an aqueous metal acetate solution were rapidly injected into the hot reaction mixture by using a syringe. The reaction mixture was held at reflux for 10 h and the samples were recovered by centrifugation and drying.

Under these conditions, TBAH shows no measurable decomposition. However, hydro/ionothermal synthesis in an autoclave has shown that at around 130 °C decomposition of TBAH begins. Under these conditions, an oily second phase develops on the surface of the reaction solution. NMR spectroscopic analyses revealed that the oil is tributylamine. As the tetrabutylammonium cation eliminates 1-butene at high temperatures,[32] the formation of tributylamine is not surprising, but it is not an issue for the conditions used in the current system.

Figure 1 and Table 1 show that in almost all cases single-phase metal oxide or hydroxide particles are obtained. Powder X-ray diffraction (XRD) results suggest that most

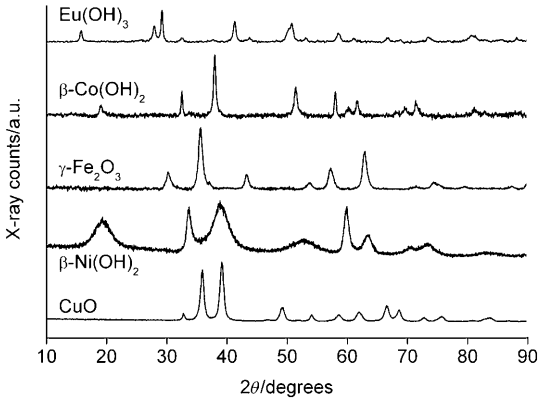

Figure 1. Representative XRD patterns of some precipitates.

Table 1. Crystal structure, morphology, and sizes, and crystallite sizes of precipitates obtained at a concentration of 0.0456 mmol of metal acetate per gram TBAH. Dimensions determined from SEM, TEM, and Rietveld refinement (crystallite sizes and anisotropy) are in nanometers. The values for other precursor concentrations are similar.[a]

Precipitate[b]	Morphology	Length or diameter	Width	Average crystallite size (anisotropy)[b]
hydrohausmannite and Mn_3O_4	disks	(78±19)		not possible
γ-Fe_2O_3 (87%) and Fe_3O_4 (23%)	cubes and spheres	(8±1)	–	Fe_2O_3: 7.58 (0.22) Fe_3O_4: 7.56 (0.22)
β-$Co(OH)_2$	disks	(215±41)	–	24.50 (19.21)
β-$Ni(OH)_2$	hexagonal plates	(15±3)	–	3.60 (2.99)
CuO	plates	(201±48)	(37±7)	10.76 (1.54)
ZnO	rods	(327±85)[c]	(29±4)[c]	24.48 (8.65)
$La(OH)_3$	spheres	(18±3)	–	5.42 (1.47)
$Ce(OH)_3$	spheres	(22±3)	–	5.25 (1.35)
$Eu(OH)_3$	rods	(241±56)	(46±6)	9.18 (6.733)
$Gd(OH)_3$	spheres[d]	(19±3)	–	14.40 (25.27)

[a] $Co(OH)_2$ is an exception, as here a clear trend can be found: at 0.0456 mmol g^{-1} TBAH the diameter is (215 ± 41) nm. The diameter decreases linearly to (145 ± 28) nm as the cobalt acetate precursor concentration is increased to 0.0910 mmol g^{-1} TBAH. [b] Data from Rietveld refinement. [c] No precipitation at 0.0456 mmol g^{-1} TBAH. Values for 0.0683 mmol g^{-1} TBAH are given instead. [d] Contains some rods.

samples consist of small particles because the reflections in the XRD pattern are broad. Where possible, Rietveld refinement (see the Supporting Information) was performed to determine the average grain size and the apparent strain. Table 1 compares the average crystallite sizes from Rietveld refinement and electron microscopy (see below). The average crystallite sizes are in most cases smaller than what is observed in electron microscopy. Rietveld refinement thus suggests that most particles do not consist of only one single crystalline domain, but consist of several primary subunits.

Figure 2 shows scanning (SEM) and transmission (TEM) electron microscopy data of some samples. SEM and TEM confirm the XRD data, as small particles are often found, although most samples contain particles that are somewhat larger than expected from XRD. Overall, TEM and XRD show that the synthesis from ionic liquid precursor (ILP)/

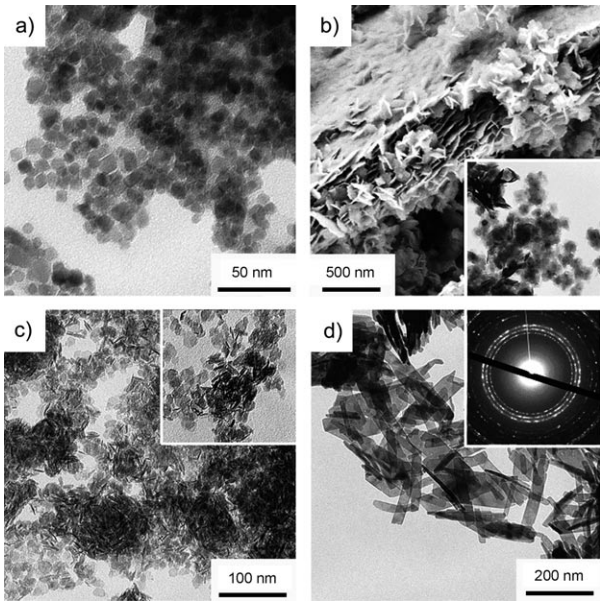

Figure 2. SEM and TEM images of a) γ-Fe_2O_3/Fe_3O_4 cubes and spheres, b) $Co(OH)_2$ plates, c) β-$Ni(OH)_2$ plates, and d) CuO plates. Inset in b) is a TEM image of the plates. Inset in c) is a magnified view of the nanoplates showing plates in top view and side view. Inset in d) is a selected-area electron diffraction pattern of the crystals shown in the image.

water mixtures provides a flexible and rapid approach for the fabrication of well-defined metal (hydr)oxide nanoparticles with uniform shapes and relatively uniform sizes.

Mn, Fe, Co, Ni, and Cu acetate in particular lead to particles with well-defined morphologies. The iron oxide particles obtained here have a well-faceted, almost cubic shape, although some spherical particles are observed as well. Most other authors report the formation of spherical particles.[33] As there are only a few reports on the fabrication of γ-Fe_2O_3 particles with diameters comparable to those presented here,[34–37] our approach is a simple and therefore technologically interesting alternative for the fabrication of well-defined γ-Fe_2O_3 nanoparticles, provided that magnetite formation can be suppressed better than is possible at the moment.

All other samples made from 3d-metal acetates have a platelike morphology. The CuO plates are up to 200 nm long and 30 to 40 nm wide. The $Ni(OH)_2$ plates have a diameter of only about 15 nm and are a few nanometers thick. There is no trend in the particle shape and size, if the concentration of the metal source (the metal acetate) is varied except for the $Co(OH)_2$ particles. Their diameter decreases with increasing acetate concentration from 215 to 145 nm. This suggests that here the acetate preferentially interacts with the side faces of the platelets and prevents further growth. This hypothesis is currently being investigated in more detail.

Electron diffraction was performed to further assess the crystallinity of the samples. It was not possible to obtain diffraction patterns from individual particles as they are either too small to generate sufficient diffraction contrast or they could not be separated from one another. Typical electron diffraction patterns display rings, which are usually assigned to polycrystalline materials. However, in the current case, the rings are not continuous, but rather consist of closely packed discrete spots. Such spotted lines are characteristic of the diffraction of an assembly of single crystalline particles with discrete orientations, where the spots of each single-crystal pattern superimpose. Further (indirect) evidence for the single crystalline nature of the particles can also be found in the fact that the particles shown in Figure 2 have a well-defined habit. Table 1 summarizes the XRD and electron microscopy data.

Examples of platelike nanocrystals, especially from CuO,[38,39] $Ni(OH)_2$ and NiO,[40–42] and $Co(OH)_2$ and Co_3O_4,[43–45] have already been reported. However, these platelets were synthesized by using different methods and none of the approaches appears to be flexible enough to construct platelike particles of all these materials using the same procedure. As a result, our ILP-based approach provides a generic approach for the controlled fabrication of a wide variety of metal (hydr)oxide nanoparticles with defined properties. Moreover, the β-$Ni(OH)_2$ plates reported here are much smaller than the smallest β-$Ni(OH)_2$ plates reported in the literature (15 vs. 50 nm).[41] Micrometer-sized Mn_3O_4 plates have also been reported,[46] but the Mn_3O_4 plates obtained in the present work are less than 100 nm.

The platelike particles obtained using our ILP approach might bring about new applications or improved performance in electrochemistry, magnetism, and catalysis. For example, our β-$Ni(OH)_2$ plates are candidates for magnetic materials or electrodes in high-density batteries.[40] The CuO, $Co(OH)_2$, Mn_3O_4, and Co_3O_4 plates could find applications in magnetic materials, heterogeneous catalysis, gas sensors, electrode materials, or in field emitters.[39,41,43–45,47]

In contrast to the 3d-element (hydr)oxides described so far, ZnO does not precipitate at the lowest acetate concentration (0.0456 mmol g^{-1} TBAH) used in this study. The inhibition of precipitation at low zinc acetate concentration is well known and is due to the formation of the tetrahydroxo zincate anion,[48] which appears to be stable and soluble under the conditions used for the mineralization in the current study. However, ZnO precipitates at higher concentrations and forms uniform crystals with well-defined hexagonal prismatic habits.

The ZnO particles obtained here are different from an earlier example by Zhu et al., in which ZnO was grown for the first time from an ILP.[16] These authors have made ZnO particles from an ILP based on various zinc–tetra(alkylamine) complexes, which were reacted with tetramethylammonium hydroxide (the methyl analogue of TBAH). The resulting particles consisted of thicker and shorter rods that often formed more complex structures like flowerlike aggregates or branched morphologies. Similar to earlier work by Endres and colleagues,[49–51] the current publication clearly shows that an exchange of the cation leads to drastically altered morphologies and dimensions of inorganics grown from ILs. However, as the zinc sources used by Zhu et al.[16]

and by us are different, it is not possible to draw quantitative conclusions on the effects of the tetraalkylammonium cation or the zinc sources.

The ZnO crystals grown under the conditions presented here are also different from other ZnO samples grown in TBAH.[17,18] In the current case, TBAH was first heated to the desired temperature and the metal acetate was dissolved in water and then injected into the hot TBAH. However, if the metal acetate is directly dissolved in TBAH and this solution is heated, the metal acetate concentrations appear to play a much larger role. In this case, at low concentrations hollow tubes form.[18] The tubes are not single crystalline, but rather aggregates of nanoparticles with a single crystal-like texture, so-called mesocrystals.[52–54] At higher concentrations the walls of the tubes become smoother, and at even higher concentrations multipod and flowerlike particles similar to the samples reported by Zhu et al.[16] form.

The presence of starch in the TBAH reaction solution completely inhibits the formation of well-defined rod or multipod particles, and instead porous, spongelike large aggregates composed of ZnO nanoparticles form.[17] These products are similar to ZnO grown from an aqueous solution in the presence of starch,[55] in the sense that in both cases ZnO nanoparticles aggregate into well-defined structures. However, TBAH as a solvent/reactant leads to extended porous architectures[17], and precipitation from an aqueous solution leads to uniform, roughly spherical particles of around 1 μm in diameter.[55]

In summary, ZnO is a useful material in the study of the effects of different precipitation conditions, because there are quite a lot of available data, even on ZnO precipitation from ionic liquids. It is also evident from the above discussion that the chemistry of the IL and the precursor (tetramethyl versus tetrabutylammonium or zinc tetra(alkylamine) versus zinc acetate precursors), the zinc precursor concentration, the reaction temperature, and the presence or absence of further growth modifiers like starch will affect particle growth. This shows that further studies into this topic are necessary to develop a quantitative understanding of how ILs control the growth of inorganic materials.

Besides d-elements, f-element (hydr)oxides and lanthanide-doped nanoparticles have also drawn considerable attention because of their unique optical, catalytic, and magnetic properties. These compounds have been widely used in various applications, including bioassays[56] and highly efficient phosphors.[57] Among other shapes, f-element hydroxide and oxide wires, sheets, and tubes have been developed.[58] Our approach yields short $Eu(OH)_3$ rods. By comparison, $Gd(OH)_3$ precipitates as a mixture of spherical particles and rods, and lanthanum and cerium hydroxide form spherical particles. These morphologies of the f-element (hydr)oxides are common. Thus, we will focus from here on the d-element oxide plates, which are less common.

Figure 3 and Table 2 show that, when 3d-element oxides are not obtained directly from the ILP, the hydroxides can be quantitatively transformed into their respective oxides by calcination at 500 °C. The line width of the XRD patterns

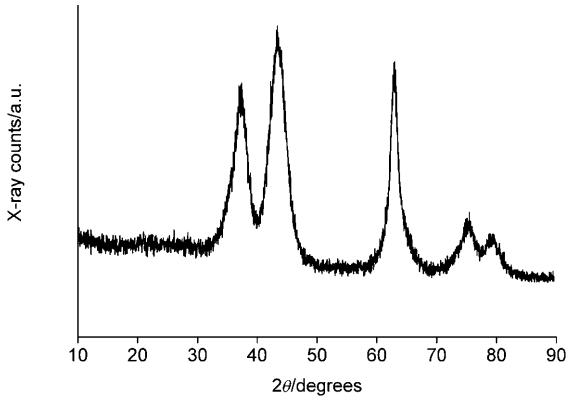

Figure 3. XRD pattern of NiO obtained from $Ni(OH)_2$ platelets after calcination at 500 °C.

Table 2. Crystal structures of precipitates after calcination at 500 °C.

Metal acetate	Product after calcination
Mn	Mn_3O_4
Co	Co_3O_4
Ni	NiO
La	La_2O_3
Ce	CeO_2
Eu	Eu_2O_3
Gd	Gd_2O_3

does not change measurably upon calcination of the hydroxide samples. This suggests that the particles do not significantly change their appearance or size, which is confirmed by Rietveld refinement of some samples. This is supported by TEM experiments (Figure 4), which show that the

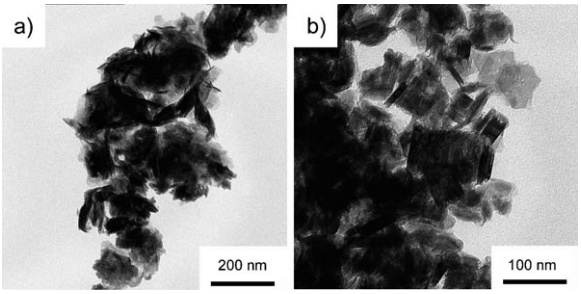

Figure 4. TEM image of a) Co_3O_4 platelets after calcination of the $Co(OH)_2$ particles at 500 °C. Compare with Figure 2b for a sample before calcination. b) Mn_3O_4 after calcination of hydrohausmannite/Mn_3O_4 at 500 °C.

$Co(OH)_2$ platelets shrink and collapse only marginally. Similarly, the hydrohausmannite plates keep their size and morphology upon calcination to Mn_3O_4. As other samples show the same behavior, we conclude that calcination does not significantly affect the particle morphology and size, which is an important factor, for example, in ceramic processing.

We also investigated the synthesis of mixed-metal compounds by examining the coprecipitation from correspond-

ing metal acetate mixtures. Figure 5 and Figure 6 show representative XRD and electron microscopy data from these samples. They demonstrate that coprecipitation of suitable

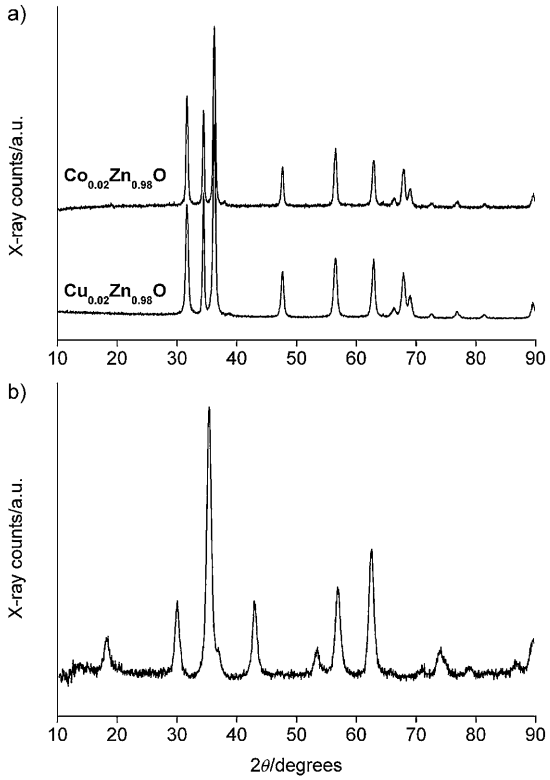

Figure 5. a) XRD patterns of Cu- and Co-doped ZnO (2 mol% Cu or Co). b) XRD pattern of $CoFe_2O_4$.

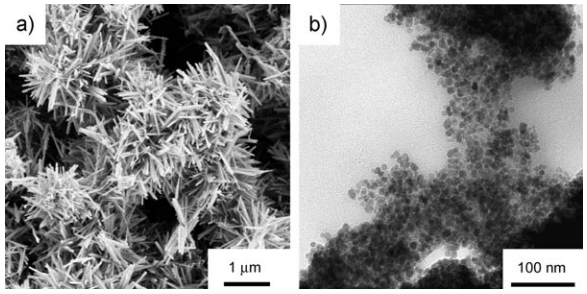

Figure 6. a) SEM image of $Cu_{0.02}Zn_{0.98}O$ rods and b) TEM image of $CoFe_2O_4$ spheres.

amounts of metal acetates in TBAH can be used to fabricate compounds like cobalt or nickel ferrite particles and doped ZnO particles. The latter can be made up to a concentration of approximately 3 mol% Cu or Co. Above this concentration, XRD reveals that a mixture of ZnO with CuO or $Co(OH)_2$, respectively, forms. This finding is, although unfortunate, in line with earlier observations.[59]

Cobalt and nickel ferrite nanoparticles are single-phase Co- and $NiFe_2O_4$, respectively, and the line broadening of the XRD patterns suggests that the particles are in both cases rather small. Indeed, Rietveld refinement of the $CoFe_2O_4$ yields an average crystallite size of 12.6 nm. The $NiFe_2O_4$ could not be refined and an average crystallite size can hence not be given.

Electron microscopy further shows that the doped ZnO particles have a well-developed needlelike crystal habit, although there is some variation in the particle dimensions. The ferrite nanoparticles are, as anticipated from XRD, small, but have a uniform shape and a rather narrow size distribution. The diameter of the $CoFe_2O_4$ particles is (11 ± 4) nm and the diameter of the $NiFe_2O_4$ particles is (8 ± 2) nm, and the sizes only marginally vary with the initial reactant concentrations. Here, XRD (12.6 nm) and TEM (11 nm) analysis of the cobalt ferrite clearly suggest that each particle consists of a single crystallite.

Figure 7 shows electron paramagnetic resonance (EPR) spectra of cobalt ferrite nanoparticles at various temperatures. The spectra have been recorded with the same micro-

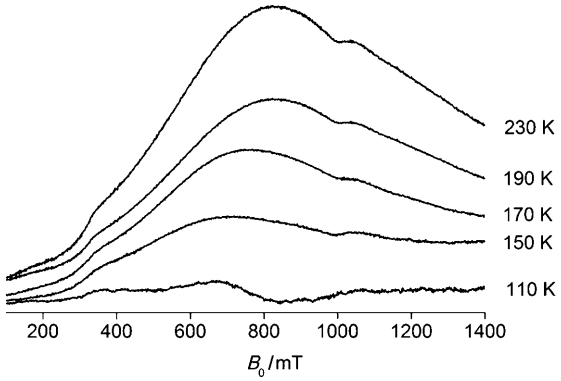

Figure 7. EPR spectra of $CoFe_2O_4$ nanoparticles measured at various temperatures. The spectra were constructed from shorter field sweeps.

wave power and unchanged receiver gain. Due to the high degree of magnetic interaction, the spectra are very broad and no more details are resolved. The thermal evolution of the EPR spectra clearly shows that the paramagnetic character of the nanoparticles decreases with decreasing temperature and collapses just above 100 K. At temperatures below approxmiately 120 K, no magnetization could be detected anymore and the signal in the EPR spectra disappears.

Figure 8 and Figure 9 show complementary data from magnetic measurements on the cobalt and nickel ferrite particles. Figure 8 shows that the cobalt ferrite particles are ferromagnetic in the whole temperature range up to around 400 K. Therefore, to limit the motion of the crystallites with the field, measurements were also done on powders embedded in poly(ethylene glycol) (PEG) and scaled to the absolute values obtained with the neat powder. The rather large difference observed between the field cooling (FC) and zero-field cooling (ZFC) data indicates a strong anisotropy. The ZFC curve of the sample in PEG is almost zero and quasi-constant between 1.8 and 100 K, which indicates that

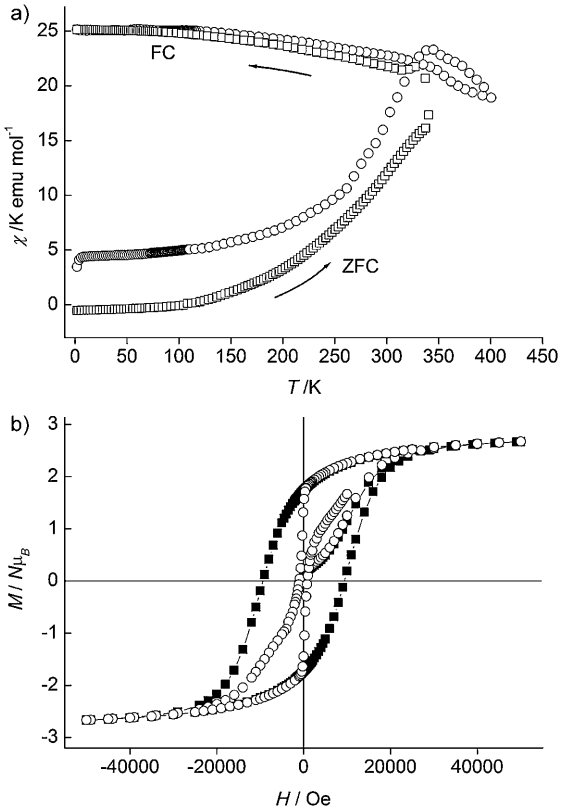

Figure 8. Magnetic data of the cobalt ferrite nanoparticles: a) χ versus T plot; FC and ZFC correspond to field cooling and zero-field cooling curves, respectively, and the arrows indicate the temperature variation; b) M versus H cycle at 1.8 K. Measurements were carried out on neat powder (○) and immobilized in poly(ethylene glycol) (■).

the cobalt ferrite particles are blocked with random direction. Above 100 K, there is a superparamagnetic regime in which the fluctuations of the magnetic moment in the small applied field result in the increase of the susceptibility joining the FC curve above room temperature. This is consistent with the EPR data, which show that the superparamagnetic signal collapses just above 100 K.

The fact that the ZFC curve increases progressively is merely due to dipolar interactions between particles that are not well isolated in the PEG matrix and to a small spreading of the blocking temperature related to the particle size distribution. The maximum of the ZFC curve corresponds to a mean blocking temperature $T_B \approx 375$ K, at which the FC and ZFC curves tend to join. This value is consistent with those observed previously for a series of slightly smaller cobalt ferrite nanoparticles.[60]

The magnetization versus field hysteresis was measured at 1.8 K (Figure 8b). Whereas the measurement of the neat powder sample shows strong motion or magnetization at the inversion of the field, the dispersion in PEG is very efficient to overcome this problem. A quite strong coercive field of around 1 T is observed ($H_C = 0.94$ T), denoting a high anisotropy as expected for cobalt ferrite nanoparticles, which are hard magnetic materials. The magnetization is almost saturated at $M = 2.7\ \mu_B$ (64.3 emu g^{-1}) under 5 T, which is of the correct order of magnitude but at the lower end of what is observed in the literature.

Figure 9 shows the same data for the nickel ferrite particles, which show a superparamagnetic behavior with a blocking temperature (T_B) of 23 K corresponding to the maximum of the ZFC curve. The Curie temperature, determined by the point at which the FC and ZFC curves split, is $T_C = 125$ K. These two values are significantly higher than those reported in the literature for particles with similar sizes.[61,62] The sharpness of the ZFC peak is consistent with the narrow size distribution observed by TEM for the nickel ferrite particles. The magnetization versus field cycle at 1.8 K (Figure 9b) exhibits a coercive field of 0.12 T. It does not totally saturate at 5 T, and extrapolation of the high field measures leads to a magnetic saturation moment $M_s = 0.8\ \mu_B$ (19.1 emu g^{-1}), which is far below the saturation magnetization of bulk nickel ferrite.[62] Similar observations on nickel ferrite particles were explained by the existence of a spin-glass-like layer at the surface and canting of the Fe^{3+} spin moment, possibly due to surface coating.[61–64]

We have also investigated the variation of the peaks of the ac susceptibility components as a function of the frequency to evaluate the relaxation time of this magnetic system. The measurements were performed on powder in PEG. As expected, the position of the maximum of ac susceptibilities, and thus the blocking temperature, increases with the alternative field frequency.

According to the Néel model for isolated single domain particles, the simplest way to determine the relaxation time as a function of temperature of superparamagnets is to define the blocking temperature (T_B^{ν}) for each frequency (ν) as the peak maximum of the out-of-phase susceptibility. Given the T_B^{ν} values from this procedure, it is possible to determine the dynamics of the particles by fitting the data to the Arrhenius law $\tau = 1/2\pi\nu = \tau_0 \exp(KV/k_B T)$, in which τ_0 is the microscopic time, K the anisotropy, and V the volume of the particles. The best fit to the Arrhenius law is shown in Figure 9d. From these data we find that $\tau_0 = 3.1 \times 10^{-23}$ s and $KV/k_B = 944$ K. Considering the mean particle size value (8 nm), the anisotropy constant was estimated at about 6 kJ m^{-3}, which is slightly higher than that for bulk nickel ferrite (5.4 kJ m^{-3}).[64] The value of τ_0 is much smaller than is typical for non-interacting assemblies of superparamagnetic nanoparticles (10^{-11}–10^{-8} s). This suggests the occurrence of strong interactions between the nanoparticles that are not well isolated in the PEG, thus mitigating the application of the Néel model in the present case.

The differences in the magnetic behavior of the cobalt and nickel ferrite particles can possibly be explained by the different sizes. Whereas the nickel ferrite particles (8 nm from TEM) are below the approximately 10 nm particle size required for superparamagnetism, the cobalt ferrite nanoparticles (11 nm from TEM, 12.6 nm from Rietveld) may be slightly too large to exhibit superparamagnetism.

Figure 10 shows the corresponding EPR spectrum of the nickel ferrite $NiFe_2O_4$ sample. The spectrum exhibits a broad, slightly distorted isotropic signal at approximately

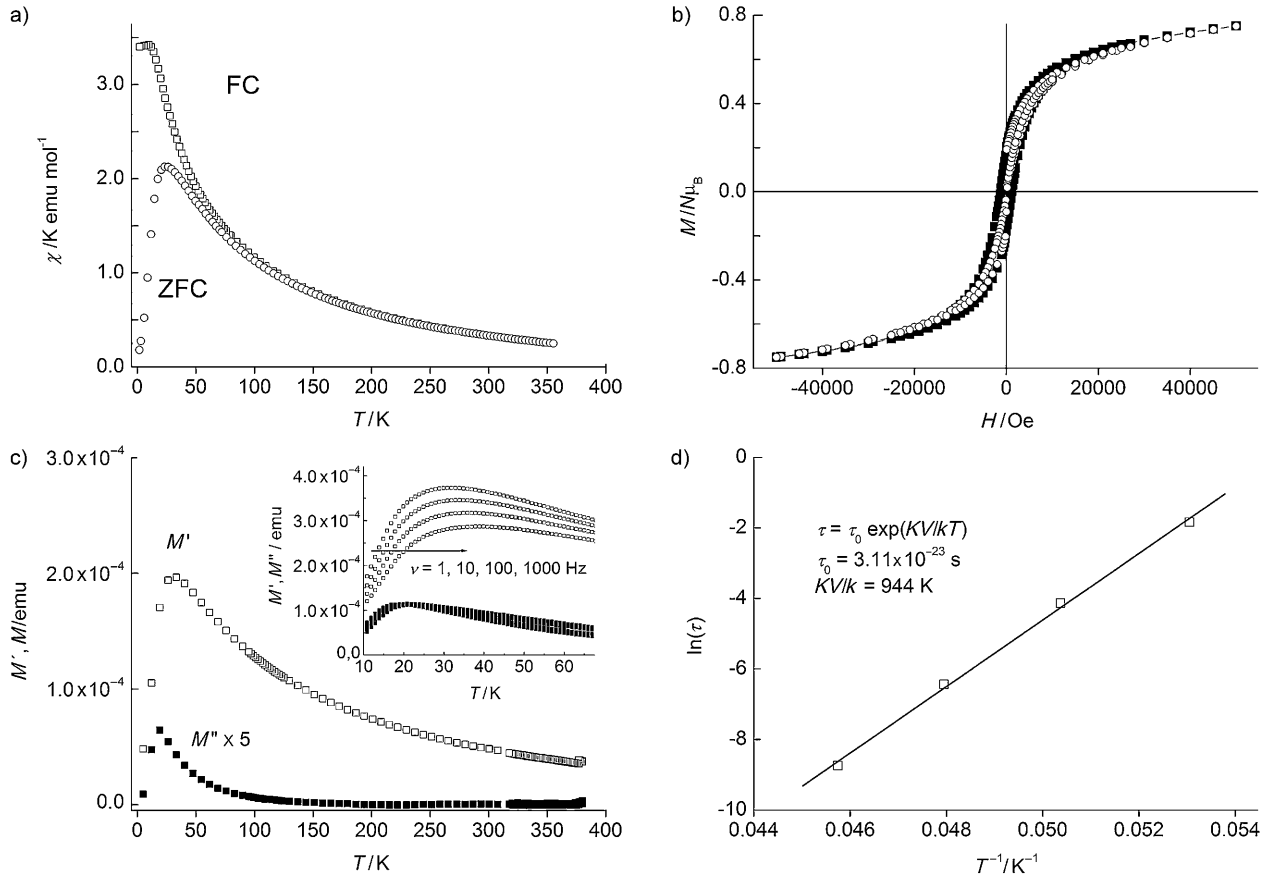

Figure 9. Magnetic data of the nickel ferrite nanoparticles: a) χ versus T plot; FC and ZFC correspond to field cooling and zero-field cooling, respectively; b) M versus H cycle at 1.8 K. Measurements were carried out on neat powder (○) and immobilized in poly(ethylene glycol) (■); c) ac susceptibility versus temperature variation and its frequency dependence in the inset; d) the corresponding $\ln(\tau)$ versus $1/T_B{}^{\nu}$ plot, with $\tau = 1/2\pi\nu$.

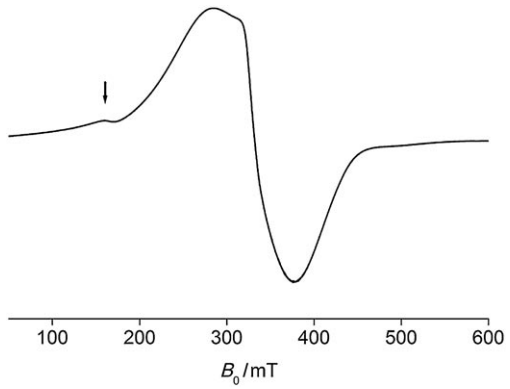

Figure 10. EPR spectrum of $NiFe_2O_4$ nanoparticles measured at 295 K. The small signal at half-field is marked with an arrow.

330 mT. The signal is broad because of magnetic interactions in the sample. The weak signal at approximately half-field (≈165 mT) is attributed to forbidden transitions with $\Delta M_s = \pm 2$. No hyperfine structure splittings are resolved, but the spectrum can be used as a fingerprint. In contrast to the cobalt ferrite spectrum shown in Figure 7, the spectrum is not temperature-sensitive and does not change significantly between room temperature and 100 K.

Conclusion

This paper is a continuation of our previous work on reactive ionic liquids as precursors for inorganic matter.[6–10,12,17,18] Here we have used water as a cosolvent to improve the solubility of the metal acetate precursors. If needed, the use of water can be avoided by choosing other metal sources like acetylacetonates, which should be soluble in the pure IL or by using tailor-made metal complexes, similar to the approach by Zhu et al.[16] The current paper shows that even a simple and seemingly imperfect ionic liquid precursor (ILP) is well suited for the efficient, rapid fabrication of single-phase inorganic powders, which in some cases have useful morphologies (mostly plates) and interesting properties. As a result, ionic liquid (crystal) precursors are a viable strategy not only for the fabrication of CuCl[7–9] or metallic[10,13] nanostructures but also for technologically important materials like metal (hydr)oxides.

Experimental Section

Powder synthesis: Tetrabutylammonium hydroxide (TBAH: N-$(C_4H_9)_4OH{\cdot}30H_2O$, m.p. 26–28 °C), $Mn(OAc)_2{\cdot}4H_2O$, $Fe(OAc)_2$, $Co(OAc)_2{\cdot}4H_2O$, $Ni(OAc)_2{\cdot}4H_2O$, $Cu(OAc)_2{\cdot}H_2O$, $Zn(OAc)_2{\cdot}2H_2O$, $La(OAc)_3{\cdot}H_2O$, $Ce(OAc)_3{\cdot}H_2O$, $Eu(OAc)_3{\cdot}H_2O$, and $Gd(OAc)_3{\cdot}H_2O$ were purchased from Aldrich and used without further purification. In a typical synthesis, tetrabutylammonium hydroxide (10 g) was heated to boiling. The respective metal acetate (0.456 mmol) was dissolved in water (2 mL) to form a clear solution. This solution was injected rapidly into the hot TBAH and the resulting mixture was held at reflux for 10 h. The mixtures became turbid after a few minutes and remained so throughout the entire reaction. The products were recovered by repeated centrifugation and washing with water and ethanol, respectively, and dried at 60 °C for 5 h. Samples were calcined at 400 to 700 °C for 1 to 10 h in air.

X-ray diffraction: XRD was done using a Nonius PDS 120 with $Cu_{K\alpha}$ radiation and a position-sensitive detector, and using a Nonius D8 with $Cu_{K\alpha}$ radiation. Rietveld refinement was performed using Fullprof version 4.00 (May 2008).[65] The peaks were fitted with a Thompson–Cox–Hastings pseudo-Voigt profile, convoluted with an axial divergence asymmetry function.[66] Instrumental resolution function was determined according to the method of Louër.[67] Strain broadening was used as implemented,[68] but the anisotropic size broadening was modeled using the Scherrer formula written as a linear combination of spherical harmonics.[69] The peak asymmetry and a simple preferential orientation correction as implemented in Fullprof were used. In some cases, a simplified and approximated refinement was performed when the quality of the XRD data was not sufficient. Atomic positions were found on the Crystallography Open Database[70] or in the literature.[71–73]

Electron microscopy: SEM was done using a Philips XL-30 ESEM scanning electron microscope operated at 10 kV, and using a LEO 1550 Gemini scanning electron microscope operated at 20 kV. Samples were sputtered with Au or Pt (Philips) or Au/Pt (LEO) prior to imaging. TEM was done using a Zeiss 912 Omega transmission electron microscope operated at 120 kV.

EPR spectroscopy: EPR spectra were recorded using a Bruker CW-EPR spectrometer E500 in X-band ($\approx$9.5 GHz) between 100 and 295 K.

Magnetic measurements: Magnetic measurements were carried out using an MPMS-XL Quantum Design SQUID magnetometer in the ranges 1.8–400 K and $\pm$5 T. The ac susceptibilty measurements were performed using a 3.5 Oe alternating field between 1 and 1000 Hz. All samples were measured as neat powders and in poly(ethylene glycol) (PEG) for blocking the motion of the powder with the magnetic field. In the latter case, the experimental values were rescaled to the absolute values of the neat powder. The highest temperature was 350 K, that is, below the melting temperature of the PEG used. Magnetic susceptibilities were measured in a 50 Oe static field using both field cooling and zero-field cooling procedures.

Acknowledgements

The authors thank R. Pitschke and H. Runge for help with electron microscopy, and the Swiss National Science Foundation, the MPI of Colloids and Interfaces, the Potsdam Graduate School (Chemical Reactions in Green Solvents: Understanding and Optimizing Sustainable Reactions), and the University of Potsdam for financial support.

[1] J. P. Jolivet, *Metal Oxide Chemistry and Synthesis: From Solution to Solid State*, Wiley, Chicester, New York, Weinheim, Brisbane, Singapore, Toronto, **2000**.
[2] L. E. Greene, B. D. Yuhas, M. Law, D. Zitoun, P. Yang, *Inorg. Chem.* **2006**, *45*, 7535.
[3] R. Seshadri, *Curr. Opin. Solid State Mater. Sci.* **2006**, *9*, 1.
[4] R. Janisch, P. Gopal, N. A. Spaldin, *J. Phys. Condens. Matter* **2005**, *17*, R657.
[5] C. Lopez, *Small* **2005**, *1*, 378.
[6] A. Taubert, *Acta Chim. Slov.* **2005**, *52*, 168.
[7] A. Taubert, C. Palivan, O. Casse, F. Gozzo, B. Schmitt, *J. Phys. Chem. C* **2007**, *111*, 4077.
[8] A. Taubert, P. Steiner, A. Mantion, *J. Phys. Chem. B* **2005**, *109*, 15542.
[9] A. Taubert, *Angew. Chem.* **2004**, *116*, 5494; *Angew. Chem. Int. Ed.* **2004**, *43*, 5380.
[10] A. Taubert, I. Arbell, A. Mecke, P. Graf, *Gold Bull.* **2006**, *39*, 205.
[11] A. Taubert, *Acta Chim. Slov.* **2005**, *52*, 183.
[12] A. Taubert, Z. Li, *Dalton Trans.* **2007**, *7*, 723.
[13] W. Dobbs, J.-M. Suisse, L. Douce, R. Welter, *Angew. Chem.* **2006**, *118*, 4285; *Angew. Chem. Int. Ed.* **2006**, *45*, 4179.
[14] C. K. Lee, C. S. Vasam, T. W. Huang, H. M. J. Wang, R. Y. Yang, C. S. Lee, I. J. B. Lin, *Organometallics* **2006**, *25*, 3768.
[15] K.-S. Kim, S. Choi, J.-H. Cha, S.-H. Yeon, H. Lee, *J. Mater. Chem.* **2006**, *16*, 1315.
[16] H. Zhu, J.-F. Huang, Z. Pan, S. Dai, *Chem. Mater.* **2006**, *18*, 4473.
[17] D. Mumalo-Djokic, W. B. Stern, A. Taubert, *Cryst. Growth Des.* **2008**, *8*, 330.
[18] Z. Li, A. Geßner, J. P. Richters, J. Kalden, T. Voss, C. Kübel, A. Taubert, *Adv. Mater.* **2008**, *20*, 1279.
[19] T. Nakashima, N. Kimizuka, *J. Am. Chem. Soc.* **2003**, *125*, 6386.
[20] E. R. Cooper, C. D. Andrews, P. S. Wheatley, P. B. Webb, P. Wormald, R. E. Morris, *Nature* **2004**, *430*, 1012.
[21] E. R. Parnham, R. E. Morris, *J. Mater. Chem.* **2006**, *16*, 3682.
[22] E. R. Parnham, R. E. Morris, *Chem. Mater.* **2006**, *18*, 4882.
[23] E. R. Parnham, R. E. Morris, *J. Am. Chem. Soc.* **2006**, *128*, 2204.
[24] E. R. Parnham, R. E. Morris, *Acc. Chem. Res.* **2007**, *40*, 1005.
[25] E. R. Parnham, P. S. Wheatley, R. E. Morris, *Chem. Commun.* **2006**, 380.
[26] H. Kaper, F. Endres, I. Djerdj, M. Antonietti, B. M. Smarsly, J. Maier, Y.-S. Hu, *Small* **2007**, *3*, 1753.
[27] M. Antonietti, D. Kuang, B. Smarsly, Y. Zhou, *Angew. Chem.* **2004**, *116*, 5096; *Angew. Chem. Int. Ed.* **2004**, *43*, 4988.
[28] T. Brezesinski, C. Erpen, K. Iimura, B. Smarsly, *Chem. Mater.* **2005**, *17*, 1683.
[29] T. Wang, H. Kaper, M. Antonietti, B. Smarsly, *Langmuir* **2007**, *23*, 1489.
[30] H. K. Farag, F. Endres, *J. Mater. Chem.* **2008**, *18*, 442.
[31] A. Orlov, A. Roy, M. Lehmann, M. Driess, S. Polarz, *J. Am. Chem. Soc.* **2007**, *129*, 371.
[32] M. E. Bos in *Encyclopedia of Reagents for Organic Synthesis* (Ed.: L. Paquette), Wiley, New York, **2004**.
[33] A. B. Bourlinos, A. Simopoulos, D. Petridis, *Chem. Mater.* **2002**, *14*, 899.
[34] K. Woo, J. Hong, S. Choi, H.-W. Lee, J.-P. Ahn, C. S. Kim, S. W. Lee, *Chem. Mater.* **2004**, *16*, 2814.
[35] A. B. Bourlinos, R. Herrera, N. Chalkias, D. Jiang, Q. Zhang, L. A. Archer, E. P. Giannelis, *Adv. Mater.* **2005**, *17*, 234.
[36] A. B. Bourlinos, A. Bakandritsos, V. Georgakilas, V. Tzitzios, D. Petridis, *J. Mater. Sci.* **2006**, *41*, 5250.
[37] L. Etgar, E. Lifshitz, R. Tannenbaum, *J. Phys. Chem. C* **2007**, *111*, 6238.
[38] C. Lu, L. Qi, J. Yang, D. Zhang, N. Wu, J. Ma, *J. Phys. Chem. B* **2004**, *108*, 17825.
[39] G. Zou, H. Li, D. Zhang, K. Xiong, C. Dong, Y. Qian, *J. Phys. Chem. B* **2006**, *110*, 1632.
[40] Z. Liang, Y. Zhu, X. Hu, *J. Phys. Chem. B* **2004**, *108*, 3488.
[41] X. Wang, L. Li, Y. Zhang, S. Wang, Z. Zhang, L. Fei, Y. Qian, *Cryst. Growth Des.* **2006**, *6*, 2163.
[42] G.-T. Zhou, Q.-Z. Yao, X. Wang, J. C. Yu, *Mater. Chem. Phys.* **2006**, *98*, 267.
[43] Y. Zhu, H. Li, Y. Koltypin, A. Gedanken, *J. Mater. Chem.* **2002**, *12*, 729.
[44] Y. Hou, H. Kondoh, M. Shimojo, T. Kogure, T. Ohta, *J. Phys. Chem. B* **2005**, *109*, 19094.

[45] Z. Liu, R. Ma, M. Osada, K. Takada, T. Sasaki, *J. Am. Chem. Soc.* **2005**, *127*, 13869.
[46] Y. Dai, K. Wang, J. Xie, *Appl. Phys. Lett.* **2007**, *90*, 104102.
[47] T. Ahmad, K. Ramanujachary, S. Lofland, A. K. Ganguli, *J. Mater. Chem.* **2004**, *14*, 3406.
[48] A. F. Hollemann, N. Wiberg, *Lehrbuch der Anorganischen Chemie*, 91st–100th ed., deGruyter, Berlin, New York, **1985**.
[49] E. M. Moustafa, S. Zein El Abedin, A. Shkurankov, E. Zschippang, A. Y. Saad, A. Bund, F. Endres, *J. Phys. Chem. B* **2007**, *111*, 4693.
[50] S. Zein El Abedin, F. Endres, *ChemPhysChem* **2006**, *7*, 58.
[51] F. Endres, S. Zein El Abedin, *Phys. Chem. Chem. Phys.* **2006**, 2101.
[52] T. Wang, H. Cölfen, M. Antonietti, *J. Am. Chem. Soc.* **2005**, *127*, 3246.
[53] M. Niederberger, H. Cölfen, *Phys. Chem. Chem. Phys.* **2006**, *8*, 3271.
[54] H. Colfen, M. Antonietti, *Angew. Chem.* **2005**, *117*, 5714; *Angew. Chem. Int. Ed.* **2005**, *44*, 5576.
[55] A. Taubert, G. Wegner, *J. Mater. Chem.* **2002**, *12*, 805.
[56] J. Feng, G. Shan, A. Maquieira, M. E. Koivunen, B. Guo, B. D. Hammock, I. M. Kennedy, *Anal. Chem.* **2003**, *75*, 5282.
[57] V. Buissette, D. Giaume, T. Gacoin, J.-P. Boilot, *J. Mater. Chem.* **2006**, *16*, 529.
[58] X. Wang, Y. Li, *Chem. Eur. J.* **2003**, *9*, 5627.
[59] D. M. Whittle, A. A. Mirzaei, J. S. J. Hargreaves, R. W. Joyner, C. J. Kiely, S. H. Taylor, G. J. Hutchings, *Phys. Chem. Chem. Phys.* **2002**, *4*, 5915.
[60] G. Baldi, D. Bonacchi, C. Innocenti, G. Lorenzi, C. Sangregorio, *J. Magn. Magn. Mater.* **2007**, *311*, 10.
[61] A. Kale, S. Gubbala, R. D. K. Misra, *J. Magn. Magn. Mater.* **2004**, *277*, 350.
[62] R. H. Kodama, A. E. Berkowitz, J. E. J. McNiff, S. Foner, *J. Appl. Phys.* **1997**, *81*, 5552.
[63] A. E. Berkowitz, J. A. Lahut, I. S. Jacobs, L. M. Levison, D. W. Forester, *Phys. Rev. Lett.* **1975**, *34*, 594.
[64] Y. Kinemuchi, K. Ishizaka, H. Suematsu, W. Jiang, K. Yatsui, *Thin Solid Films* **2002**, *407*, 109.
[65] J. Rodriguez-Carvajal, *Phys. B* **1993**, *192*, 55.
[66] P. Thompson, D. E. Cox, J. B. Hastings, *J. Appl. Crystallogr.* **1987**, *20*, 79.
[67] D. Louer, J. I. Langford, *J. Appl. Crystallogr.* **1988**, *21*, 430.
[68] J. Rodriguez-Carvajal, M. T. Fernandez-Diaz, J. L. Martinez, *J. Phys. Condens. Matter* **1991**, *3*, 3215.
[69] M. Jarvinen, *J. Appl. Crystallogr.* **1993**, *26*, 525.
[70] For the Crystallography Open Database, see: http://cod.ibt.lt/.
[71] D. R. Dillin, W. O. Milligan, R. J. Williams, *J. Appl. Crystallogr.* **1973**, *6*, 492.
[72] D. F. Mullica, J. D. Oliver, W. O. Milllgan, *Acta Cryst. B* **1979**, *35*, 2668.
[73] M.-W. Beall, W. O. Milligan, H. A. Wolcott, *J. Inorg. Nucl. Chem.* **1977**, *39*, 65.

Received: January 18, 2008
Published online: July 30, 2008

